

Suzaku View of the Supernova Remnant RCW 86: X-Ray Studies of Newly-Discovered Fe-Rich Ejecta

Hiroya YAMAGUCHI^{1,2} Katsuji KOYAMA³ and Hiroyuki UCHIDA³

¹Harvard-Smithsonian Center for Astrophysics, 60 Garden Street, Cambridge, MA 02138, U.S.A.

hyamaguchi@head.cfa.harvard.edu

²RIKEN (The Institute of Physical and Chemical Research), 2-1 Hirosawa, Wako, Saitama 351-0198, Japan

³Department of Physics, Kyoto University, Kitashirakawa-Oiwake-cho, Sakyo, Kyoto 606-8502, Japan

(Received 2011 July 28; accepted 2011 September 5)

Abstract

We report on results of imaging and spectral analysis of the supernova remnant (SNR) RCW 86 observed with Suzaku. The SNR is known to exhibit K-shell emission of low ionized Fe, possibly originating from supernova ejecta. We revealed the global distribution of the Fe-rich plasma in the entire remnant, for the first time; the Fe-K emission was clearly detected from the west, north, and south regions, in addition to the X-ray brighter shells of southwest and northeast, where the presence of the Fe-rich ejecta has already been reported. The spectrum of each region is well represented by a three-component model consisting of low- and high-temperature thermal plasmas and a non-thermal emission. The lower-temperature component, with elemental abundances of near the solar values, likely originates from the forward shocked interstellar medium, while the Fe-rich ejecta is described by the hotter plasma. From the morphologies of the forward and reverse shocks in the west region, the total ejecta mass is estimated to be $1\text{--}2M_{\odot}$ for the typical explosion energy of $\sim 1 \times 10^{51}$ erg. The integrated flux of the Fe-K emission from the entire SNR roughly corresponds to a total Fe mass of about $1M_{\odot}$. Both of these estimates suggest a Type Ia supernova origin of this SNR. We also find possible evidence of an Fe-rich clump located beyond the forward-shock front in the north rim, which is reminiscent of ejecta knots observed in the Tycho and Vela SNRs.

Key words: ISM: individual (RCW 86) — supernova remnants — X-rays: spectra

1. Introduction

Making the most of its high spectral sensitivities especially in the hard (> 5 keV) X-ray band, recent Suzaku observations of extended X-ray sources have continuously provided unique results: e.g., the Fe-K line diagnostics of the Galactic center plasma (Koyama et al. 2007a), the first firm detection of the Fe-K α line from SN 1006 (Yamaguchi et al. 2008a), and the discoveries of low-abundance elements (Cr, Mn, and/or Ni) from the supernova remnant (SNR) Tycho (Tamagawa et al. 2009) and the Perseus cluster (Tamura et al. 2009). The Galactic SNR RCW 86, the remnant of SN 185 (e.g., Pisarski et al. 1984), is another interesting object where the Suzaku performance can be highly utilized, as its spectrum exhibits weak K-shell emission from low ionized Fe.

The origin of the Fe-K α emission in RCW 86 had been long-standing issue since the discovery. Judging from its center energy of 6.4 keV (consistent with that of neutral Fe) together with the presence of hard X-rays, Vink et al. (1997) proposed that the emission originates from fluorescence caused by supra-thermal electrons. However, Bocchino et al. (2000), Bamba et al. (2000), and Borkowski et al. (2001b) argued its origin of low ionized ejecta, because the spectrum showed the Fe abundance of significantly higher than the solar value. They also revealed that the hard X-ray emission does not originate from the supra-thermal bremsstrahlung but non-

thermal synchrotron emission from relativistic electrons.

The Chandra observation of the southwest (SW) region, the brightest rim of the SNR, successfully resolved spatial distribution of the thermal and non-thermal components (Rho et al. 2002). The non-thermal emission is located at the inward region with respect to the optical and soft thermal X-ray filaments of the swept-up interstellar medium (ISM). It was suggested, therefore, that the relativistic electrons are accelerated at the reverse shock in this region. This is in distinct contrast to typical shell-like SNRs, such as SN 1006 and Tycho where non-thermal X-rays are observed close to the blast waves (e.g., Koyama et al. 1995; Hwang et al. 2002). In addition, the Fe-K α emission was revealed to be localized at the SNR's interior, supporting strongly its origin of the reverse-shocked ejecta. This result was confirmed by the Suzaku long-exposure observation (Ueno et al. 2007). The authors also found that the center energy of the Fe-K α line is slightly higher than that for the neutral Fe, suggesting that the emission originates from the high-temperature plasma in an extremely low ionization state.

The northeast (NE) region, the second brightest rim, is another site where the detection of the Fe-K α emission had been reported (ASCA; Tomida et al. 1999). However, the following observations by XMM-Newton and Chandra failed to detect the emission line (e.g., Vink et al. 2006). Using Suzaku, Yamaguchi et al. (2008b) firmly confirmed the presence of the emission and revealed its spatial dis-

Table 1. Observation log.

Region	Obs. ID	Obs. start date	(RA, Dec) _{J2000}	Exposure	SCI*
SW	500004010	2006 February 12	(220.2761, -62.6782)	101 ks	off
NE	501037010	2006 August 12	(221.2555, -62.3618)	60 ks	off
West	503001010	2009 February 2	(220.2753, -62.4270)	54 ks	on
North	503002010	2009 January 29	(220.4956, -62.2074)	55 ks	on
South	503003010	2009 January 31	(220.8315, -62.6734)	55 ks	on
SE/BGD	503004010	2009 February 1	(221.3859, -62.6710)	54 ks	on

*Spaced-low Charge Injection (Uchiyama et al. 2009).

tribution. It has no spatial correlation with the thermal and non-thermal X-ray filaments of the blast wave, but is enhanced at the inner region. This is another piece of evidence that the emission originates from the Fe-rich ejecta.

To date, detailed X-ray studies on RCW 86 were mostly limited in the SW and NE regions.¹ This is likely because these two rims are particularly bright in hard X-rays originating from the synchrotron radiation. However, since the preceding studies suggest that the Fe-K α emission is not related to the supra- nor non-thermal electrons but is due to the thermal emission from the shocked ejecta (e.g., Rho et al. 2002; Yamaguchi et al. 2008b), it should be observed in other X-ray faint regions as well. In this paper, we report the first detection of Fe-rich ejecta from the entire remnant, including the west, north, and south rims. It should be emphasized that the origin of RCW 86 (i.e., Type Ia or core-collapse supernova) is not revealed yet. Since the production of Fe in Type Ia supernovae is far larger than that of core-collapse ones (e.g., Nomoto et al. 1984; Iwamoto et al. 199), measurement of its abundance is one of the essential clues to classify the progenitor type. Although RCW 86 is extremely intriguing source for studies of the non-thermal phenomena (e.g., Aharonian et al. 2009; Helder et al. 2009), we here concentrate mainly on the thermal emission, and detailed results concerning the non-thermal X-rays will be presented in a separate paper (A. Bamba et al., in preparation).

We assume the distance to the SNR of 2.8 kpc (e.g., Westerlund 1969; Rosado et al. 1996) throughout the paper. The errors quoted in the text and tables are at the 90% confidence level, and the error bars in the figures are for 1σ confidence, unless otherwise stated.

2. Observation and Data Screening

Six pointings were made on RCW 86 with Suzaku in 2006 and 2009 to cover almost the entire region of the SNR. Observation logs are found in table 1. The details of the earlier two observations, SW and NE, are reported by Ueno et al. (2007) and Yamaguchi et al. (2008b), respectively. Here, we present results on the other regions obtained with X-ray Imaging Spectrometers (XIS), but the SE region was used only as the background data.

The XIS consists of four sensors. Three of them (XIS0, XIS2, and XIS3) are installed with front-illuminated (FI) charge-coupled devices (CCDs) whose characteristics are almost identical with each other, while the other (XIS1) is installed with a back-illuminated (BI) CCD (Koyama et al. 2007b). However, the XIS2 was out of operation during the observations in 2009 due to damage possibly caused by the impact of a micrometeorite.² The XISs were operated in normal full-frame clocking mode for all the observations. For the data analysis, we used the standard tools of HEADAS version 6.10. We reprocessed the public data using `xispi` software and the latest calibration database (CALDB) released on 2011 February 10. The data were reduced in accordance with the standard screening criteria.³ Only grade 0, 2, 3, 4, and 6 events were used in the following analysis.

3. Results

In figure 1, we show the three-color XIS image of the SNR, where the exposure and vignetting are corrected. Red, blue, and green represent 0.6–2.0 keV (soft), 3.0–5.5 keV (hard), and 6.3–6.5 keV (Fe-K), respectively. As already reported by Ueno et al. (2007) and Yamaguchi et al. (2008b), the Fe-K emission is observed at the SNR’s interior of the SW and NE regions. In addition, we can see similar Fe-K features in the other field of view (FoV). There is no correlation between the spatial distributions of the Fe-K α and hard X-ray components, which rejects the possibility of the fluorescence origin for the Fe-K α emission as was once suggested by Vink et al. (1997).

We extracted XIS spectra from the entire FoV of each region. The result is shown in figure 2, where the spectra of the two FIs (XIS0 and XIS3) are summed up after the subtraction of non X-ray backgrounds (NXB; generated by the `xisnxbgen` software). All the spectra clearly show the Fe-K α lines. The large equivalent widths (EW) are observed in the West (~ 570 eV) and North (~ 480 eV) regions, while the South region shows smaller EW (~ 150 eV) because of considerably large contamination by the non-thermal X-rays from the SW rim (e.g., Rho et al. 2002). We hence present detailed imaging and spectral analysis for the West and North regions in the following subsections.

¹ Spectroscopic results for the north rim were reported by several authors (e.g., Bocchino et al. 2000; Vink et al. 2006), but there is no published report regarding the west and south rims.

² <http://heasarc.nasa.gov/docs/suzaku/analysis/abc/node8.html>

³ http://heasarc.nasa.gov/docs/suzaku/processing/criteria_xis.html

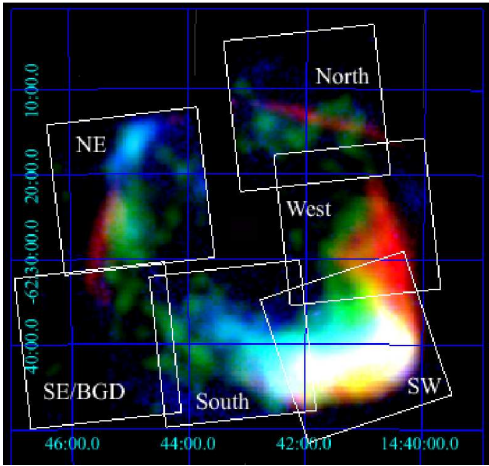


Fig. 1. Three-color XIS image of RCW 86 with a logarithmic scale on the surface brightness. Red, blue, and green contain emissions from 0.6–2.0 keV (soft), 3.0–5.5 keV (hard), and 6.3–6.5 keV (Fe-K), respectively. The coordinates (RA and Dec) refer to epoch J2000.0. The FoVs of the XIS are indicated by the white squares. The data from the three active XIS are combined, but those of the four corners, irradiated by the ^{55}Fe instrumental calibration sources, are removed from the Fe-K image. The exposure and vignetting effect are corrected after the subtraction of the NXB.

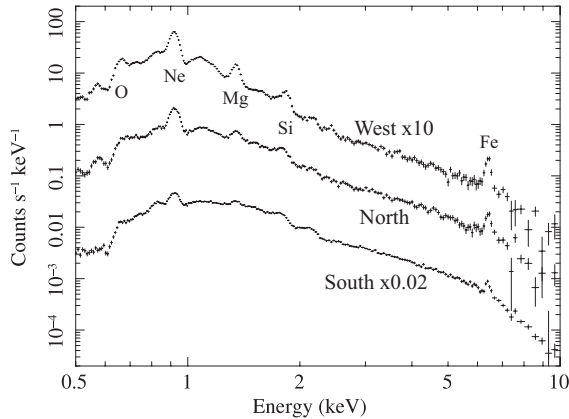


Fig. 2. XIS-FI spectra extracted from each FoV, of which the normalizations are modified.

3.1. West region

The three-color image of the West region is shown in figure 3, where the corresponding energy ranges are the same as figure 1. The soft and hard band images were binned by each 8×8 pixels and smoothed with a Gaussian kernel of $\sigma = 24$ pixel ($\approx 25''$). On the other hand, the Fe-K image was binned by each 32×32 pixels (to improve the statistics) with a smoothing Gaussian kernel of $\sigma = 96$ pixel ($\approx 100''$). The soft emission is spatially coincident with the Balmer-dominated optical filament (Smith 1997), a signature of a blast wave propagating in a tenuous region. Similarly to the SW and NE regions, the Fe-K emission is apparently enhanced at the inner region against the soft filament. Projection profiles of the soft and Fe-K

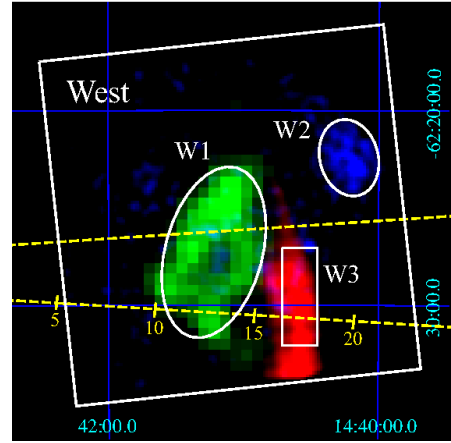


Fig. 3. Three-color image of the West region. The scale is linear. Red, blue, and green contain emissions from 0.6–2.0 keV, 3.0–5.5 keV, and 6.3–6.5 keV, respectively. The ellipses and rectangle are the regions used in our spectral analysis. The yellow dashed lines with the radius scale (in arcmin) indicate the region where the projection profiles (figure 4) are extracted.

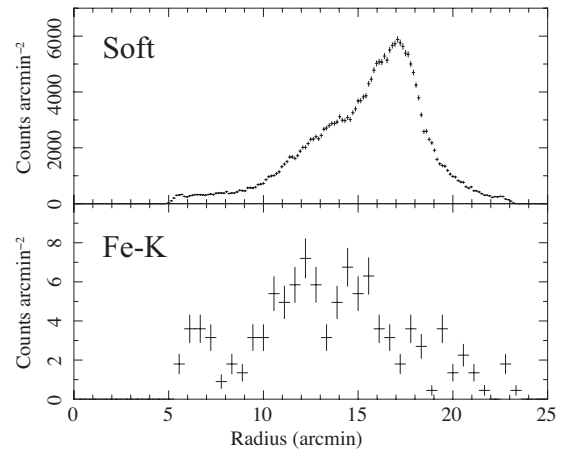


Fig. 4. Projection profiles of the Soft (upper) and Fe-K (lower) band for the West region. The center of the SNR is assumed to be $(\text{RA}, \text{Dec})_{\text{J2000}} = (220.77, -62.47)$.

emissions are given in figure 4, where $(\text{RA}, \text{Dec})_{\text{J2000}}$ of $(220.77, -62.47)$ is assumed to be the SNR's geometrical center. In addition, we can see the diffuse hard emission extending outward to the soft rim. This emission has the radio counterpart (Whiteoak & Green 1996; Dickel et al. 2001), and hence likely originates from non-thermal X-rays.

We extracted the XIS spectra from three characteristic regions shown in figure 3: W1, W2, and W3, hereafter. The background spectra for all the data were taken from the $5' \times 10'$ rectangle region in the SE FoV. Although several different background regions were attempted, the following results did not essentially change. The background-subtracted spectra of the W1 region are shown in figure 5. We first analyzed the 4–10 keV band by fitting with a power-law and a Gaussian. The center

Table 2. Best-fit parameters for the W1 region.

Components	Parameters	Model A	Model B
Absorption*	N_{H} (cm^{-2})	$2.9 (\pm 0.3) \times 10^{21}$	$2.8 (\pm 0.3) \times 10^{21}$
VPSHOCK	kT_e (keV)	0.46 ± 0.02	$0.46^{+0.03}_{-0.02}$
(ISM)	τ_u (cm^{-3} s)	$6.6^{+0.9}_{-0.6} \times 10^{10}$	$6.8^{+1.0}_{-0.6} \times 10^{10}$
	O (solar)	$0.78^{+0.05}_{-0.06}$	$0.76^{+0.06}_{-0.07}$
	Ne (solar)	1.4 ± 0.1	1.3 ± 0.1
	Mg (solar)	0.71 ± 0.04	0.72 ± 0.04
	Fe (solar)	$0.70^{+0.05}_{-0.04}$	$0.70^{+0.05}_{-0.04}$
	$n_e n_{\text{H}} dl$ (cm^{-5}) [†]	$6.0^{+0.1}_{-0.2} \times 10^{17}$	$6.0^{+0.2}_{-0.5} \times 10^{17}$
VNEI	kT_e (keV)	5.0 (fixed)	
(Ejecta)	τ (cm^{-3} s)	1.0×10^9 (fixed)	
	$n_e n_{\text{Fe}} dl$ (cm^{-5}) [†]	$1.7^{+0.2}_{-0.3} \times 10^{13}$	$1.7 (\pm 0.3) \times 10^{13}$
Non-thermal	$\Gamma / \nu_{\text{rolloff}}$ (Hz)	3.0 ± 0.1	$4.6^{+0.6}_{-0.7} \times 10^{16}$
	Norm [‡]	$5.1^{+0.4}_{-0.6} \times 10^{-5}$	$4.0 (\pm 0.1) \times 10^{-2}$
χ^2/dof		437/280	435/280

*tbabs model (Wilms et al. 2000).

[†] dl is emission depth.

[‡]Differential flux ($\text{photons s}^{-1} \text{cm}^{-2} \text{keV}^{-1}$) at 1 keV in Model A, while Flux density in unit of Jy at 1 GHz in Model B.

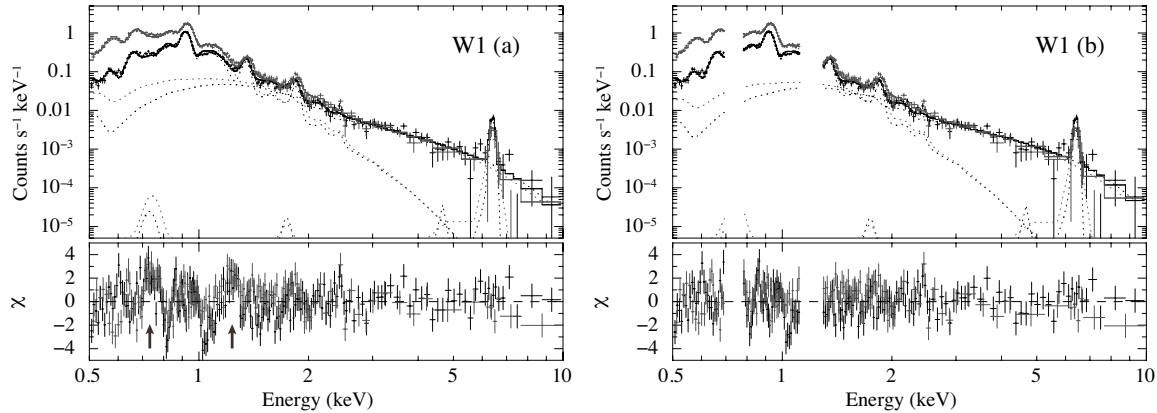


Fig. 5. (a) XIS spectra extracted from the W1 region. The black and gray represent the FI and BI, respectively. The best-fit model components are given with the dashed lines. The energies where the large residuals are seen (0.73 keV and 1.2 keV) are indicated with black arrows. (b) Same as (a), but where the problematic energy ranges (0.70–0.78 keV and 1.13–1.28 keV) are ignored when fitted (see text for details).

energy of the Fe-K line was determined to be 6403^{+21}_{-19} eV, suggesting that the ionization state of the Fe is less than +19 (e.g., Makishima 1986; Kallman et al. 2004). The obtained EW of $2.7 (\pm 0.5)$ keV requires the Fe abundance of at least 5 solar for a non equilibrium ionization (NEI) plasma with an electron temperature of 2.0–10 keV, which is typical range for young SNRs. This is the robust evidence that the emission originates from the Fe-rich ejecta.

The result of the imaging analysis (figure 3) implies that the full-band X-ray spectrum of RCW 86 consists of at least three independent components: two plasmas responsible to the soft and Fe-K emissions plus a non-thermal component. We hence used a plane-parallel shock model (vpshock model; Borkowski et al. 2001a) to describe the soft thermal component, while the Fe-K emis-

sion was reproduced by a simpler model of an NEI plasma with a single ionization parameter (vnei model⁴). Free parameters of each component are given in table 2. For the soft component, abundances of heavy elements other than O, Ne, Mg, and Fe were fixed to the solar values of Anders & Grevesse (1989). For the Fe-K (vnei) component, we made an assumption that the plasma consists only of Fe ions and electrons without protons or other heavy elements.⁵ Since the center energy of the Fe-K line

⁴ http://space.mit.edu/home/dd/Borkowski/APEC_nei_README.txt

⁵ If we run a fit allowing the Fe abundance to vary freely, an extremely large value (>100 solar) of the abundance is required. This causes difficulty in the determination of both the absolute abundance and emission measure, since the bremsstrahlung associated with Fe ions contributes significantly to the continuum emission.

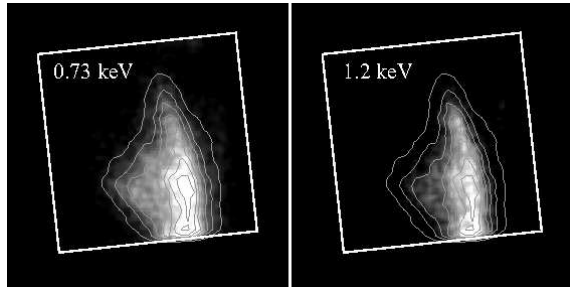


Fig. 6. Gray scale images of the West rim in the energy bands of 0.7–0.78 keV (left) and 1.13–1.28 keV (right). The intensity contours of the Ne IX $K\alpha$ emission are overlaid.

(6403 eV) corresponds to the ionization parameter (τ) of $\sim 1 \times 10^9 \text{ cm}^{-3} \text{ s}$ in the wide temperature range of 2–10 keV, we fixed it to this value. On the other hand, the electron temperature (kT_e) is difficult to be constrained because the continuum in the hard X-ray band is likely to be dominated by the non-thermal component. Therefore, we assumed $kT_e = 5 \text{ keV}$, following Rho et al. (2002). For the non-thermal component, we used a simple power-law (Model A) or an `srcut` model (Model B). In the latter case, the energy index in the radio band was fixed to $\alpha = 0.6$ according to Green (2009). In addition, we allowed for a small offset in the photon energy to the pulse-height gain relationship only for the BI data, since the absolute gain of the XIS has an uncertainty of a few eV (Koyama et al. 2007b). The offset values required for the various regions were about -10 eV , within the allowable range of the calibration error.

These models and assumptions resulted the best-fit `vpshock` temperature and ionization parameter of $kT_e = 0.49 (\pm 0.03) \text{ keV}$ and $\tau_u = 4.7 (\pm 0.3) \times 10^{10} \text{ cm}^{-3} \text{ s}$, respectively. However, the fit was not satisfied with a large χ^2/dof value of 659/328 (for Model A) or 673/328 (for Model B). Although we attempted to add another spectral component, the fit was not improved significantly with this procedure. There are remarkable disagreements between the data and model around the energies of $\sim 0.73 \text{ keV}$ and $\sim 1.2 \text{ keV}$ (see figure 5a). If we allowed the electron temperature and ionization parameter of the `vnei` component to vary freely, the residuals around these energy were reduced. This process, however, required a larger τ value (for the `vnei` component) of 7.0 (6.8–7.3) $\times 10^9 \text{ cm}^{-3} \text{ s}$. This corresponds to the Fe-K center energy of $\sim 6.44 \text{ keV}$, inconsistent with the measured value ($6403_{-19}^{+21} \text{ eV}$). Therefore, the spectral excesses are unlikely to be associated with the Fe-K emission, but seem to originate from the soft thermal (`vpshock`) component. To confirm this, we made the narrow band images in 0.70–0.78 keV and 1.13–1.28 keV (figure 6) and compared with the intensity contours of the Ne IX $K\alpha$ line (0.87–0.94 keV), the major component of the soft component. Both the images show apparently the same morphology as the Ne IX $K\alpha$ emission, supporting that the $\sim 0.73 \text{ keV}$ and $\sim 1.2 \text{ keV}$ excesses are associated with the soft emission.

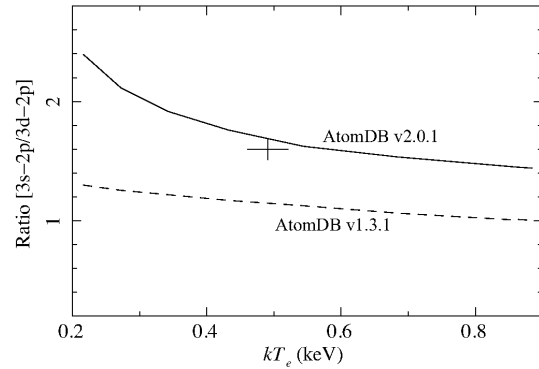


Fig. 7. Emissivity ratio of Fe XVII 3s→2p (0.73 keV) to 3d→2p (0.82 keV) lines calculated using the latest AtomDB (version 2.0.0; solid) and previous one (version 1.3.1; dashed), as a function of the electron temperature. The observed ratio from the W1 spectrum is shown as the black cross, where the error bars are for 90% confidence.

As the origin of the 0.73 keV emission, either O VII K-shell lines of $n \geq 4$ to 1 or Fe XVII L-shell lines of 3s→2p is considered. Yamaguchi et al. (2008a) found a similar 0.73 keV feature in the spectrum of SN 1006, and pointed out that this is likely to be due to the high-level K-shell transitions ($K\delta$, $K\epsilon$, $K\zeta$, etc.) of O VII which are missing from conventional NEI codes. In SN 1006, an ionization timescale is quite low ($\tau \sim 5 \times 10^9 \text{ cm}^{-3} \text{ s}$) and an electron temperature is moderate ($kT_e \sim 0.5 \text{ keV}$), so that the contribution of the O VII K-shell series cannot be ignored. In our case, however, the fluxes of these lines are negligibly small compared to those of the O VIII emissions because of the higher ionization timescale ($\tau_u \sim 5 \times 10^{10} \text{ cm}^{-3} \text{ s}$). Therefore, we can eliminate the possibility that the 0.73 keV excess comes from O VII emissions absent in the plasma code. Meanwhile, Katsuda et al. (2011) recently suggested that charge-exchange process between O VIII ions and neutrals can induce the strong emissions of O VII $n \geq 4$ to 1 transitions. They comprehensively analyzed Suzaku and XMM-Newton data of Cygnus Loop and found that the 0.73 keV flux is enhanced in several rim regions. However, the charge exchange emissions should be (if any) observed only in the outermost rims (Katsuda et al. 2011; Lallement 2004), and hence unlike in our case.

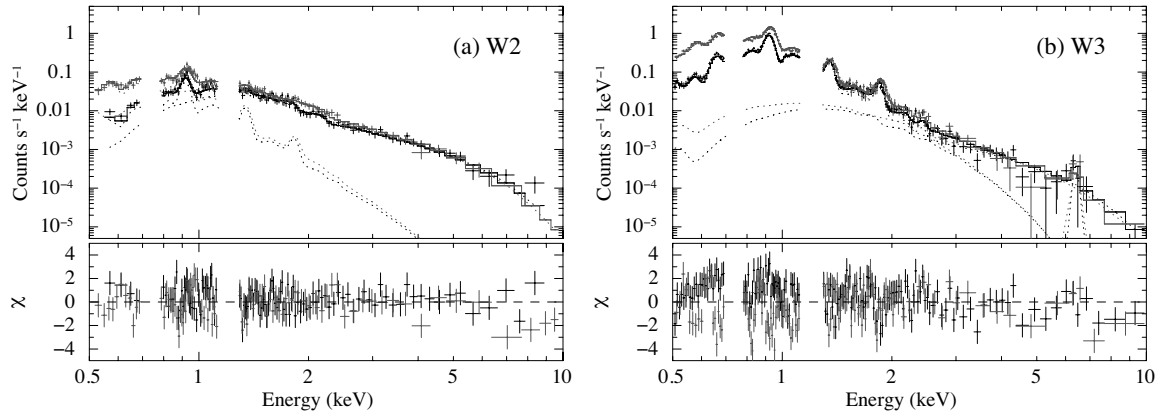
We thus associate the 0.73 keV feature that we see in the RCW 86 spectrum with the Fe XVII L-shell emissions. As argued in some previous works (e.g., N103B: van der Heyden et al. 2002; SNR 0509–67.5: Warren & Hughes 2004), the emissivity ratio between the Fe XVII 3s→2p ($\sim 730 \text{ eV}$) to 3d→2p ($\sim 820 \text{ eV}$) transitions is uncertain, which often causes a failure to reproduce the data around these energies. In figure 7, we show the 3s→2p/3d→2p emissivity ratios calculated using AtomDB⁶ version 1.3.1 (which is involved in the `vnei` model we used) and recently-updated version 2.0.0. The updated database predicts the ratio about twice higher than that

⁶ <http://www.atomdb.org/>

Table 3. Best-fit parameters for the W2 and W3 regions.

Components	Parameters	W2		W3	
		Model A	Model B	Model A	Model B
Absorption	N_{H} (10^{21} cm $^{-2}$)	3.4 ± 0.3	$3.3^{+0.2}_{-0.3}$	2.9 ± 0.2	$2.9^{+0.3}_{-0.2}$
VPSHOCK	kT_e (keV)	$0.50^{+0.08}_{-0.05}$	$0.50^{+0.05}_{-0.04}$	$0.54^{+0.02}_{-0.03}$	0.55 ± 0.02
	τ_u (10^{10} cm $^{-3}$ s)	$1.5^{+1.3}_{-0.7}$	$1.7^{+0.5}_{-0.3}$	5.4 ± 0.5	$5.4^{+0.8}_{-0.4}$
	O (solar)	1*	1*	$0.58^{+0.05}_{-0.04}$	$0.58^{+0.05}_{-0.04}$
	Ne (solar)	1*	1*	$1.0^{+0.05}_{-0.04}$	1.0 ± 0.1
	Mg (solar)	1*	1*	0.56 ± 0.03	$0.56^{+0.04}_{-0.03}$
	Fe (solar)	1*	1*	$0.44^{+0.02}_{-0.03}$	0.44 ± 0.03
	$n_e n_{\text{H}} dl$ (10^{17} cm $^{-5}$)	$2.0^{+1.6}_{-1.0}$	$2.0^{+0.5}_{-0.3}$	$15.6^{+0.2}_{-0.4}$	$16.0^{+0.6}_{-0.5}$
VNEI	$n_e n_{\text{Fe}} dl$ (10^{12} cm $^{-5}$)	—	—	$3.7^{+3.1}_{-3.5}$	4.0 ± 3.4
Non-thermal	$\Gamma / \nu_{\text{rolloff}}$ (10^{16} Hz)	3.1 ± 0.1	$3.7^{+0.7}_{-0.5}$	3.0*	4.6*
	Norm †	1.9 ± 0.2	$0.19^{+0.05}_{-0.04}$	$0.52^{+0.05}_{-0.06}$	0.04 ± 0.01
χ^2/dof		229/194	220/194	613/268	611/268

*Fixed values.

 † Units are 10^{-4} photons s $^{-1}$ cm $^{-2}$ keV $^{-1}$ (at 1 keV) and Jy (at 1 GHz) in Model A and Model B, respectively**Fig. 8.** Same as figure 5, but for the W2 (a) and W3 (b) regions. The energy ranges of 0.70–0.78 keV and 1.13–1.28 keV are ignored.

of the previous one. The primary reason of this change is that the updated one takes into account the dielectronic recombination process, in addition to the electron-impact excitation, as the source of the L-shell line emissions. In the figure, we also plot the 3s–2p/3d–2p flux ratio determined from the W1 spectra. This was derived by fitting the 0.5–1.0 keV spectra with an ad hoc model consisting of a `vnei` component with the abundance of Fe fixed to zero and three Gaussians at 0.73, 0.82, and 0.90 keV (for the Fe L-shell blends). The obtained ratio of 1.62 ± 0.09 is almost consistent with the value expected by the updated atomic code at $kT_e \sim 0.5$ keV. Therefore, the excess seen around 0.73 keV is reasonably explained by the uncertainty of the Fe XVII emissivities in the currently-distributed NEI model.

Regarding the excess of the data at 1.2 keV, Rho et al. (2002) reported the presence of a similar spectral feature in the Chandra data of RCW 86 SW rim. They argued that this was possibly due to the Fe XVII blend of $n \geq 6$ to 2

that were missing from an NEI code they used. Although the atomic database that we used in our analysis includes the electron excitations in the Fe XVII ions up to the level of $n = 7$, the excess at this energy still remains. The origin of this feature is therefore debatable. Nevertheless, it is worth noting that the positive correlation between the 1.2 keV flux and Fe abundance has been confirmed by the spatially-resolved spectral analysis on the Cygnus Loop (H. Uchida et al., in preparation, where the same plasma code is used). We consider, therefore, that the 1.2 keV feature is also related to the Fe XVII L-shell emissions, or the Ni L-shell blend would be an alternative possibility. Ignoring the energy ranges of 0.70–0.78 keV and 1.13–1.28 keV (figure 5b), we obtained the best-fit parameters given in table 2. Although the χ^2/dof value (~ 1.6) is still unacceptable from a statistical point of view, we did not apply further complicated models.

We next analyzed the spectra of W2 and W3 regions shown in figure 8. The problematic energy ranges of 0.70–

Table 4. Best-fit parameters for the N1 and N2 regions.

Components	Parameters	N1		N2	
		Model A	Model B	Model A	Model B
Absorption	N_{H} (10^{21} cm $^{-2}$)	5.3 ± 0.3	$5.0^{+0.4}_{-0.6}$	$5.4^{+0.6}_{-0.2}$	$5.5^{+0.2}_{-0.4}$
VPSHOCK	kT_e (keV)	$0.27^{+0.02}_{-0.07}$	$0.34^{+0.08}_{-0.05}$	$0.27^{+0.02}_{-0.06}$	0.27 ± 0.03
	τ_u (10^{10} cm $^{-3}$ s)	$7.9^{+1.9}_{-1.3}$	$5.0^{+1.9}_{-1.8}$	$4.5^{+0.4}_{-0.5}$	4.6 ± 0.9
VNEI	$n_e n_{\text{H}} dl$ (10^{17} cm $^{-5}$)	$8.4^{+7.2}_{-2.7}$	$4.8^{+2.6}_{-2.1}$	$20.7^{+19.7}_{-2.7}$	$21.9^{+9.5}_{-2.4}$
	$n_e n_{\text{Fe}} dl$ (10^{13} cm $^{-5}$)	1.0 ± 0.3	1.1 ± 0.3	1.0 ± 0.4	1.0 ± 0.5
Non-thermal	$\Gamma / \nu_{\text{rolloff}}$ (10^{16} Hz)	3.2 ± 0.1	$3.4^{+0.6}_{-0.5}$	3.2 ± 0.1	$3.3^{+0.8}_{-0.6}$
	Norm*	1.1 ± 0.1	$0.11^{+0.04}_{-0.03}$	$1.2^{+0.2}_{-0.1}$	0.13 ± 0.04
χ^2/dof		351/213	349/213	174/166	173/166

*Units are 10^{-4} photons s $^{-1}$ cm $^{-2}$ keV $^{-1}$ (at 1 keV) and Jy (at 1 GHz) in Model A and Model B, respectively

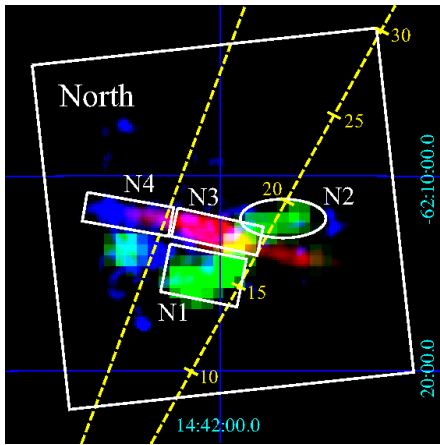


Fig. 9. Same as figure 3, but for the North rim. The regions used in the spectral analysis are indicated with the ellipse and rectangles. The yellow dashed lines show the region where the projection profiles (figure 10) are extracted.

0.78 keV and 1.13–1.28 keV were excluded from these spectra as well. Since the W2 spectrum exhibits no feature of the Fe-K emission, we did not include the hotter *vnei* component. Moreover, the flux of the soft thermal component is too weak to obtain a reasonable fit with a lot of free parameters, we fixed all the elemental abundances of this component to unity. For the W3 spectrum, all the parameters listed in table 3 were allowed to vary freely at first. The best fit was, however, obtained with an extremely steep slope of the non-thermal component, $\Gamma = 4.5$ in Model A or $\nu_{\text{rolloff}} = 6 \times 10^{15}$ Hz in Model B. This is unrealistic because the extrapolated radio flux is required to be ~ 3.0 Jy at 1 GHz, more than one order of magnitude higher than that of the W2 region, resulting considerable disagreement with the radio observation (Dickel et al. 2001). Therefore, we fixed the slope and roll-off frequency as those obtained in the W1 region. The results are given in table 3. The relatively large χ^2/dof values for the W3 spectrum are mainly caused by the inconsistency between the FI and BI data below 1 keV. This is probably due to incomplete calibration information for the contamination layer on the optical blocking filter in

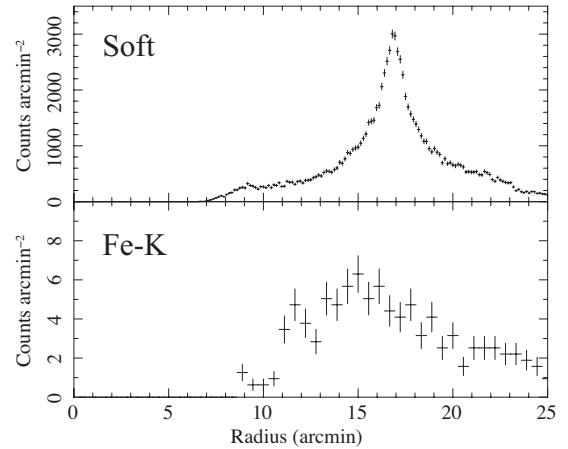


Fig. 10. Same as figure 4, but for the North region.

front of the CCDs (Koyama et al. 2007b).

3.2. North region

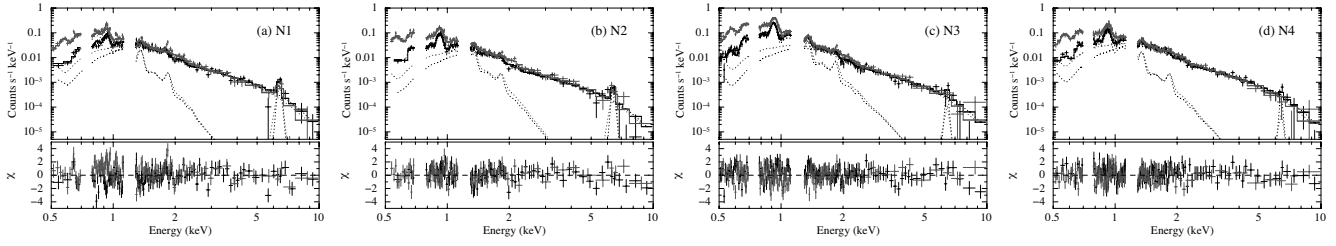
Figure 9 shows the image of the North FoV. The three colors correspond to the same energies as those in figures 1 and 3. This region is observed to have a mixture of Balmer-dominated and radiative filaments in the optical band (Smith 1997), suggesting that the blast wave is expanding into the inhomogeneous ISM. Along the filament from west to east, predominant X-ray emission process seems to change from thermal to non-thermal radiation. The most remarkable Fe-K emission is observed just behind the soft-thermal filament, analogous to the nature of the NE rim region (Yamaguchi et al. 2008b). In addition, we can see a knotty Fe-K emission located beyond the blast wave boundary. The radial profiles of the Soft and Fe-K emissions are shown in figure 10.

The spectra were extracted from four regions shown in figure 9. We subtracted the same background as was used in subsection 3.1. The results are shown in figure 11. The Fe-K α emission is clearly detected in the N1 and N2 regions, and also seen in the N3 and N4 spectra although less significant. All the spectra were fitted with the three-component model consisting of the

Table 5. Best-fit parameters for the N3 and N4 regions.

Components	Parameters	N3		N4	
		Model A	Model B	Model A	Model B
Absorption	N_{H} (10^{21} cm $^{-2}$)	$4.6^{+0.6}_{-0.4}$	$4.5^{+0.6}_{-0.4}$	$4.5^{+0.6}_{-0.7}$	$4.0^{+0.6}_{-0.9}$
VPSHOCK	kT_e (keV)	$0.36^{+0.05}_{-0.07}$	0.38 ± 0.06	$0.31^{+0.11}_{-0.05}$	$0.38^{+0.14}_{-0.07}$
	τ_u (10^{10} cm $^{-3}$ s)	$5.0^{+1.2}_{-1.1}$	$4.6^{+1.1}_{-1.0}$	$5.4^{+3.4}_{-2.5}$	$3.7^{+2.3}_{-1.2}$
	O (solar)	1.2 ± 0.2	$1.2^{+0.2}_{-0.1}$	$1.3^{+0.3}_{-0.2}$	$1.1^{+0.3}_{-0.2}$
	Ne (solar)	1.7 ± 0.2	1.6 ± 0.2	1.9 ± 0.5	$1.8^{+0.6}_{-0.3}$
	$n_e n_{\text{H}} dl$ (10^{17} cm $^{-5}$)	$9.6^{+8.9}_{-3.3}$	$9.1^{+6.5}_{-3.2}$	$7.3^{+8.0}_{-4.4}$	$4.6^{+4.9}_{-2.8}$
VNEI	$n_e n_{\text{Fe}} dl$ (10^{12} cm $^{-5}$)	$3.9^{+3.6}_{-3.4}$	$4.8^{+3.6}_{-3.4}$	$2.6^{+4.3}_{-2.6}$	$2.6^{+4.4}_{-2.6}$
Non-thermal	$\Gamma / \nu_{\text{rolloff}}$ (10^{16} Hz)	3.2 ± 0.1	$3.3^{+0.8}_{-0.6}$	3.2 ± 0.1	$3.1^{+0.7}_{-0.5}$
	Norm*	1.5 ± 0.1	$0.15^{+0.06}_{-0.04}$	2.2 ± 0.2	$0.23^{+0.07}_{-0.01}$
χ^2/dof		297/253	299/253	227/230	225/230

*Units are 10^{-4} photons s $^{-1}$ cm $^{-2}$ keV $^{-1}$ (at 1 keV) and Jy (at 1 GHz) in Model A and Model B, respectively

**Fig. 11.** Same as figure 5, but for the N1 (a), N2 (b), N3 (c), and N4 (d) regions.

soft thermal (*vpshock*), Fe-K (*vnei*), and non-thermal emissions. Again, the problematic energy ranges (0.70–0.78 keV and 1.13–1.28 keV) were ignored in the fitting, and the electron temperature and ionization timescale for the *vnei* component were assumed to be $kT_e = 5.0$ keV and $n_e t = 1 \times 10^9$ cm $^{-3}$ s, respectively. In the N1 and N2 spectra, all the abundances in the *vpshock* component were fixed to be the solar values. The best-fit parameters are given in tables 4 and 5. There is no significant spatial variation in any spectral parameters other than the normalization of each component. Bocchino et al. (2000) argued that the spectra of the North region obtained with BeppoSAX and ROSAT can be described by a single temperature NEI model with $kT_e \sim 3$ keV. We found, however, that this model failed to reproduce our data, but the multi-component model is certainly needed.

4. Discussion

4.1. Ejecta mass estimation

Since the west rim (W3 region) of RCW 86 is Balmer-dominated (Smith 1997), it is likely that the blast wave has been propagated in the low-density and relatively uniform ISM. Assuming the emission depth dl of 4.7 pc, about one-third of the blast wave radius R_{bw} of 14 pc ($= 17'$), we estimate the proton density n_{H} to be 0.3 cm $^{-3}$. Thus, the pre-shock ambient density is $n_0 = n_{\text{H}}/4 = 0.075$ cm $^{-3}$. Note that when the effect of the particle acceleration is unignorable, the value of n_0 can be smaller, but it does

not largely affect the following results.

Comparing with a numerical calculation of SNRs' dynamical evolution, we can estimate the total mass of the ejecta, M_{ej} . We here simply assume that the SNR ejecta with a constant density profile is expanding in an uniform ISM. Since the SNR's age is known to be ~ 1820 yr, the dimensionless age t^* , defined by Truelove & McKee (1999), is obtained as

$$t^* \simeq 1.8 \left(\frac{n_0}{0.075 \text{ cm}^{-3}} \right)^{1/3} \left(\frac{E_0}{10^{51} \text{ erg}} \right)^{1/2} \left(\frac{M_{\text{ej}}}{M_{\odot}} \right)^{-5/6}, \quad (1)$$

where E_0 is the explosion energy. According to the formulas in table 5 of Truelove & McKee (1999), the ratio of the reverse shock to blast wave radii $R_{\text{rs}}/R_{\text{bw}}$ can be calculated as the function of the ejecta mass. The results for representative explosion energies are given in figure 12. Assuming that the reverse shock is located at the inner edge of the Fe-K emission (W1 region), the reverse shock radius R_{rs} is approximated to be 8 pc ($= 10'$; see also figure 4), resulting $R_{\text{rs}}/R_{\text{bw}} = 0.58$. We obtain the the ejecta mass of $\sim 1.1M_{\odot}$, $\sim 1.7M_{\odot}$, and $\sim 2.1M_{\odot}$ for the cases of $E_0 = 5 \times 10^{50}$ erg, 1×10^{51} erg, and 5×10^{51} erg, respectively. Differently from the west region, the north rim of the SNR is interacting with a nonuniform dense wind-blown shell (Smith 1997; Vink et al. 1997). Nevertheless, we try a similar investigation to evaluate the uncertainty on the ejecta mass estimation. From figure 10, the ratio $R_{\text{rs}}/R_{\text{bw}}$ is obtained to be 0.65. This gives the ejecta mass

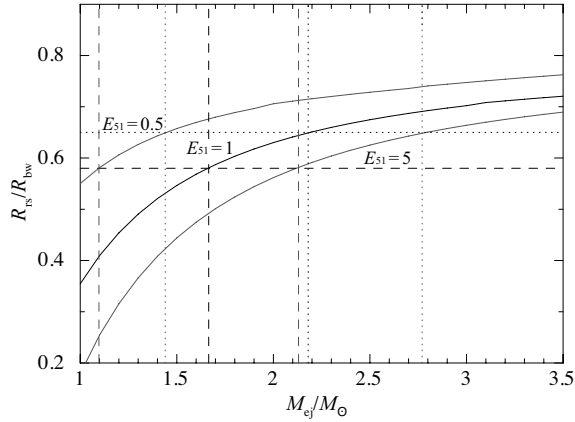


Fig. 12. Ratio of the reverse shock radius (R_{rs}) to the blast wave radius (R_{bw}) as a function of the ejecta mass (M_{ej}), calculated using the formulas of Truelove & McKee (1999). E_{51} is the explosion energy in the unit of 10^{51} erg. The observed values of R_{rs}/R_{bw} in the West and North regions of RCW 86 are indicated as the horizontal dashed and dotted lines, respectively.

of $(1.4\text{--}2.8)M_{\odot}$, not so far from the result on the west region. Investigation into the east rim (Yamaguchi et al. 2008b) also results the same estimation as the north.

Although the above estimation is derived with a number of assumptions and simplifications (i.e., uniform ambient and ejecta structures inside the cavity wall, symmetrical explosion, and so on)⁷, the estimated ejecta mass likely suggests a Type Ia origin of RCW 86. If this is not the case, at least, the remnant originates from a core-collapse explosion of a massive star whose envelope had been largely ejected by the pre-explosion stellar wind activity. This is not surprising because the SNR is suggested to be expanding in the wind-blown cavity (e.g., Vink et al. 1997).

From the integrated spectrum of the entire remnant, we measure the total flux of the Fe-K α emission to be 1.7×10^{-4} photon $\text{cm}^{-2} \text{s}^{-1}$. This corresponds to the emission measure $n_e n_{\text{Fe}} V$ of $4.2 \times 10^{53} \text{ cm}^{-3}$ (V is the emitting volume) for the $kT_e = 5$ keV case. Although the density distribution of the Fe-rich plasma is highly uncertain, we simply assume that the plasma is uniformly distributed in the spherical shell with inner and outer radii of 8 pc and 11 pc, respectively. Then, the Fe density and mass are roughly estimated to be $n_{\text{Fe}} = 2 \times 10^{-3} a^{-0.5} \text{ cm}^{-3}$ and $M_{\text{Fe}} = 9a^{-0.5} M_{\odot}$, respectively, where a is the number of electron per Fe ion. Since the value of a is in the range of 1–19 (if the pure-Fe plasma is assumed), the Fe mass should be of the order of $1M_{\odot}$. This estimation would be additional evidence supporting that the remnant originates from a Type Ia supernova rather than a core-collapse supernova where the amount of the Fe production is usually less than about $0.1M_{\odot}$.

⁷ It should also be noted that the recent work by Williams et al. (2011) suggests that the explosion center of the remnant is offset from the geometric center, whereas we assume both are consistent with each other.

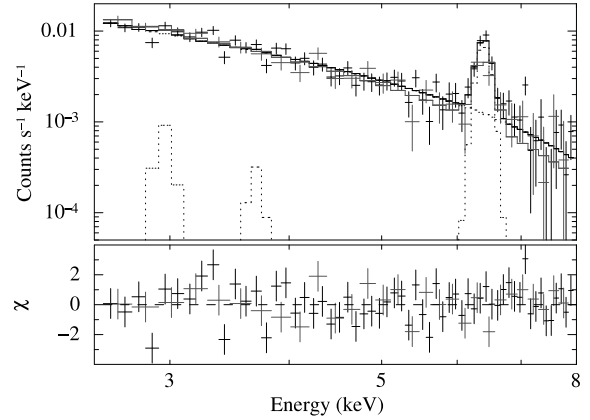


Fig. 13. NXB-subtracted 2.5–8.0 keV spectra where the data from the W1 and N1 regions are integrated. The black and gray represent the FI and BI, respectively. Detection of the Ar (2.96 keV) and Ca (3.69 keV) lines is not significant.

(e.g., Thielemann et al. 1996).

A Type Ia explosion inside a low-density cavity is quite unusual from the observational point of view (Badenes et al. 2007). However, if the mass accretion rate from the companion star is high enough, the accreting white dwarf can blow off a strong optically-thick wind (Hachisu et al. 1996; 1999). Badenes et al. (2007) argued that this outflow excavates a large cavity around the progenitor. This can be the case for RCW 86, if the SNR really originates from a Type Ia supernova. Alternatively, it is possible that the stellar winds from the other nearby massive stars had created the surrounding cavity prior to the explosion, since the remnant is located near the OB association (Westerlund 1969; Rosado et al. 1996).

4.2. Chemical composition of the ejecta component

Whether the origin of RCW 86 is Type Ia or core-collapse, substantial amounts of intermediate-mass elements (i.e., Si and S) should be observed similarly to other young SNRs. However, we find no evidence for such yields in the ejecta (vnei) component. Since these elements tend to be laid closer to the contact discontinuity, they can be considerably mixed with the shocked ISM, or the electron temperature of this layer is too low to emit detectable emission lines. On the other hand, higher- Z elements, such as Ar and Ca, are generally synthesized in a rather deep layer of Si burning where a part of ^{56}Ni is also synthesized. Therefore, emission from these elements could be detectable. Here, we search for K α lines of Ar and Ca in the W1 and N1 spectra, where the contribution of non-thermal component is relatively small compared to the other rim regions. To measure the intensities as precise as possible, we subtract only the NXB instead of using the BGD spectrum from the SE FoV, and fit phenomenologically the 2.5–8.0 keV spectra with three Gaussians and a power-law. The ionization states of both the elements are assumed to be almost neutral, so that we fix the center energies to be 2.96 keV and 3.69 keV for Ar and Ca, respectively. An absorption column of $N_{\text{H}} = 3.0 \times 10^{21} \text{ cm}^{-2}$

Table 6. Flux of emission lines.

Region	Flux (10^{-6} photon cm^{-2} s^{-1})			Flux ratio	
	Ar	Ca	Fe	Ar/Fe	Ca/Fe
W1	0.71 (<1.8)	0.12 (<0.90)	7.0 ± 0.97	<0.26	<0.13
N1	0.047 (<0.55)	0.005 (<0.38)	1.4 ± 0.40	<0.38	<0.27
W1+N1	0.75 (<2.1)	0.24 (<1.1)	9.0 ± 1.3	<0.23	<0.12

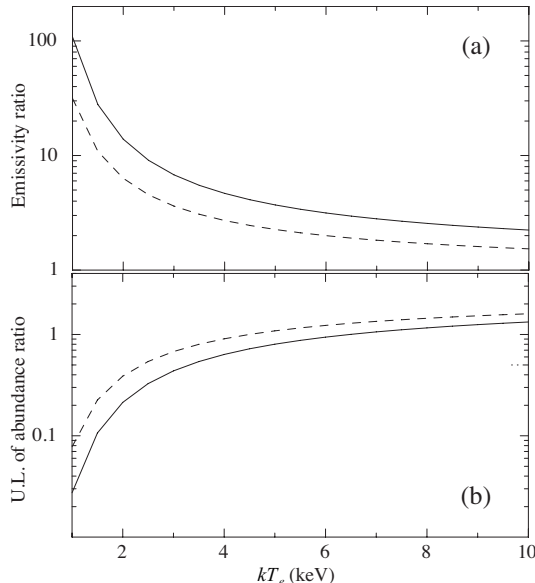


Fig. 14. (a) Emissivity ratios of $\varepsilon_{\text{Ar}}/\varepsilon_{\text{Fe}}$ (solid) and $\varepsilon_{\text{Ca}}/\varepsilon_{\text{Fe}}$ (dashed) as a function of the electron temperature. (b) Upper limits for the relative abundances of Ar/Fe (solid) and Ca/Fe (dashed) determined from the W1+N1 spectrum.

is assumed, but it does not largely affect the X-ray flux in the examined energy band. The line fluxes and ratios to that of the Fe-K line we obtained are given in table 6. Neither Ar nor Ca line is detected significantly, although we have analyzed also the integrated spectra of the W1 and N1 regions (figure 13).

Using the obtained flux ratios, we can estimate the upper limits for the abundances of Ar and Ca relative to Fe. The K-shell line emissivities $\varepsilon_Z(kT_e)$ of the element Z is calculated as

$$\varepsilon_Z(kT_e) \propto \int_{I_Z}^{\infty} f_{kT_e}(E') \cdot \sqrt{E'} \cdot \sigma_Z(E') \cdot \omega_Z \cdot dE', \quad (2)$$

where f_{kT_e} , I_Z , σ_Z , and ω_Z are the Maxwell-Boltzmann distribution function $2\sqrt{E}/[\pi(kT_e)^3] \exp(-E/kT_e)$, the K-shell ionization potential and collisional cross section, and the probability of the fluorescent emission, respectively. We follow the semi-empirical model by Quarles (1976) for the term of σ_Z , with an assumption that the cross section for the collisional innershell ionization does not severely depend on the ionization state in the range from neutral to Ne-like. For the values of ω_Z , we use the calculations by Kaastra & Mewe (1993). As the result, the emissivity ratios and upper limits of the relative abundances are derived (as a function of the electron

temperature) as shown in figures 14a and 14b, respectively. Note that the latter is determined from the merged W1+N1 spectrum. Unfortunately, the electron temperature of the ejecta component cannot be constrained by the spectral analysis, because the hard X-ray continuum of this SNR seems to be dominated by the non-thermal radiation. However, given that most young SNRs have an electron temperature of less than 10 keV, we can reject the possibility that the relative abundances of Ar/Fe and Ca/Fe are larger than 1.6 solar. This is not incompatible with the predicted yields for Type Ia supernovae.

4.3. Possible evidence of the ejecta knot

In the north region, we have observed the Fe-K emission visible beyond the blast wave filament (the N2 region in Figure 9). This feature is quite distinct from those of the other ejecta distribution in this SNR; the Fe-rich ejecta are usually observed inside the main shell that is dominated by the soft thermal emission. Therefore, different interpretation for its origin should be considered. Here we analogize it with ejecta bullets associated with the Tycho SNR or the Vela SNR, the metal-rich clumps located outside the blast-shock boundary (e.g., Tycho: Vancura et al. 1995; Decourchelle et al. 2001; Vela: Aschenbach et al. 1995; Miyata et al. 2001). Since the optical observations of RCW 86 had suggested that the blast wave in the North region is expanding into the dense inhomogeneous ISM (Smith 1997), it is likely that the shock had decelerated very recently, resulting that the ejecta knot overran the primary blast wave. If this is the case, a bow-shock feature can be observed at the head of the knot, similarly to the Vela shrapnels. However, the statistics of our data is too poor to investigate such detailed structure. Deeper observation will help reveal the origin of this peculiar Fe-K emission.

5. Summary

We have presented the first detection of Fe-K emission from the west, north, and south regions of the SNR RCW 86. Detailed imaging and spectral analysis have been performed for the former two regions. The spatial distributions of the Fe-K α and hard X-ray emissions are not correlated with each other, rejecting the possibility that the Fe-K α emission originates from the fluorescence by supra-thermal electrons or hard X-rays. In the west rim, the Fe-K emission is apparently enhanced at the inward region with respect to the forward shock, which supports its origin of supernova ejecta heated by the reverse shock. From the derived ambient density (0.075 cm^{-3})

and radii of the forward and reverse shocks (14 pc and 8 pc, respectively), the total ejecta mass is roughly estimated to be $(1-2)M_{\odot}$. This suggests that the SNR originates from a Type Ia supernova explosion rather than a core-collapse one considered previously (e.g., Rosado et al. 1996). The total mass of Fe, of the order of $1M_{\odot}$, also supports its Type Ia origin. The low-density cavity surrounding the Type Ia progenitor is not usual. It could be formed by so-called accretion winds from the progenitor itself or the outflow from the other nearby OB stars. In the north rim, we find another Fe-K emission located beyond the primary blast wave boundary, which is analogous to the ejecta fragments observed in the Tycho and Vela SNRs. To confirm its nature more conclusively, a future deep observation is required. No significant evidence for low-ionized Ar and Ca emissions is observed. This constrains the relative abundances of Ar/Fe and Ca/Fe to be less than ~ 1.6 solar.

Note—After the first submission of this paper, the results on the same object had been reported by Williams et al. (2011; arXiv:1108.1207). They presented the infrared and X-ray observations and arrived at a similar interpretation, a Type Ia origin of this remnant.

The authors deeply appreciate a number of constructive suggestions from the anonymous referee. We also thank to Drs. Adam Foster and Randall K. Smith for providing useful information about AtomDB, and Drs. Patrick O. Slane and Daniel Patnaude for stimulating discussion. Dr. Midori Ozawa largely contributed to planning the mapping observation of RCW 86 using Suzaku. H.Y. and H.U. are supported by Japan Society for the Promotion of Science (JSPS) Research Fellowship for Research Abroad and Young Scientists, respectively. K.K. is supported by the Challenging Exploratory Research program (No. 20654019) of the Ministry of Education, Culture, Sports, Science and Technology (MEXT).

References

- Aharonian, F., et al. 2009, ApJ, 692, 1500
 Anders, E., & Grevesse, N. 1989, Geochim. Cosmochim. Acta, 53, 197
 Aschenbach, B., Egger, R., & Trümper, J. 1995, Nature, 373, 587
 Badenes, C., Hughes, J. P., Bravo, E., & Langer, N. 2007, ApJ, 662, 472
 Bamba, A., Koyama, K., & Tomida, H. 2000, PASJ, 52, 1157
 Bocchino, F., Vink, J., Favata, F., Maggio, A., & Sciortino, S. 2000, A&A, 360, 671
 Borkowski, K. J., Lyerly, W. J., & Reynolds, S. P. 2001a, ApJ, 548, 820
 Borkowski, K. J., Rho, J., Reynolds, S. P., & Dyer, K. K. 2001b, ApJ, 550, 334
 Dickel, J. R., Strom, R. G., & Milne, D. K. 2001, ApJ, 546, 447
 Decourchelle, A., Sauvageot, J. L., Audard, M., et al. 2001, A&A, 365, L218
 Green, D. A., 2009, ‘A Catalogue of Galactic Supernova Remnants (2009 March version)’, Astrophysics Group, Cavendish Laboratory, Cambridge, United Kingdom <<http://www.mrao.cam.ac.uk/surveys/snrs/>>
 Hachisu, I., Kato, M., & Nomoto, K. 1996, ApJL, 470, L97
 Hachisu, I., Kato, M., & Nomoto, K. 1999, ApJ, 522, 487
 Helder, E. A., et al. 2009, Science, 325, 719
 van der Heyden, K. J., Behar, E., Vink, J., Rasmussen, A. P., Kaastra, J. S., Bleeker, J. A. M., Kahn, S. M., & Mewe, R. 2002, A&A, 392, 955
 Hwang, U., Decourchelle, A., Holt, S. S., & Petre, R. 2002, ApJ, 581, 1101
 Iwamoto, K., Brachwitz, F., Nomoto, K., Kishimoto, N., Umeda, H., Hix, W. R., & Thielemann, F.-K. 1999, ApJS, 125, 439
 Kaastra, J. S., & Mewe, R. 1993, A&AS, 97, 443
 Kallman, T. R., Palmeri, P., Bautista, M. A., Mendoza, C., & Krolik, J. H. 2004, ApJS, 155, 675
 Katsuda, S., et al. 2011, ApJ, 730, 24
 Koyama, K., Petre, R., Gotthelf, E. V., Hwang, U., Matsuura, M., Ozaki, M., & Holt, S. S. 1995, Nature, 378, 255
 Koyama, K., et al. 2007a, PASJ, 59, S245
 Koyama, K., et al. 2007b, PASJ, 59, S23
 Lallement, R. 2004, A&A, 422, 391
 Makishima, K. 1986, The Physics of Accretion onto Compact Objects, ed. Mason, K. P., Watson, M. G., & White, N. E. (Berlin: Springer), 266, 249
 Miyata, E., Tsunemi, H., Aschenbach, B., & Mori, K. 2001, ApJL, 559, L45
 Nomoto, K., Thielemann, F.-K., & Yokoi, K. 1984, ApJ, 286, 644
 Pisarski, R. L., Helfand, D. J., & Kahn, S. M. 1984, ApJ, 277, 710
 Quarles, C. A. 1976, Phys. Rev. A, 13, 1278
 Rho, J., Dyer, K. K., Borkowski, K. J., & Reynolds, S. P. 2002, ApJ, 581, 1116
 Rosado, M., Ambrocio-Cruz, P., Le Coarer, E., & Marcelin, M. 1996, A&A, 315, 243
 Smith, R. C. 1997, AJ, 114, 2664
 Tamagawa, T., et al. 2009, PASJ, 61, S167
 Tamura, T., et al. 2009, ApJL, 705, L62
 Thielemann, F.-K., Nomoto, K., & Hashimoto, M.-A. 1996, ApJ, 460, 408
 Tomida, H., Koyama, K., & Yamauchi, S. 1999, Astron. Nachr. 320, 342
 Truelove, J. K., & McKee, C. F. 1999, ApJS, 120, 299
 Ueno, M., et al. 2007, PASJ, 59, S171
 Uchiyama, H., et al. 2009, PASJ, 61, S9
 Vancura, O., Gorenstein, P., & Hughes, J. P. 1995, ApJ, 441, 680
 Vink, J., Kaastra, J. S., & Bleeker, J. A. M. 1997, A&A, 328, 628
 Vink, J., Bleeker, J., van der Heyden, K., Bykov, A., Bamba, A., & Yamazaki, R. 2006, ApJ, 648, L33
 Warren, J. S., & Hughes, J. P. 2004, ApJ, 608, 261
 Westerlund, B. E. 1969, AJ, 74, 879
 Whiteoak, J. B. Z., & Green, A. J. 1996, A&AS, 118, 329
 Wilms, J., Allen, A., & McCray, R. 2000, ApJ, 542, 914
 Yamaguchi, H., et al. 2008a, PASJ, 60, S141
 Yamaguchi, H., Koyama, K., Nakajima, H., Bamba, A., Yamazaki, R., Vink, J., & Kawachi, A. 2008b, PASJ, 60, S123